nature communications

Article

https://doi.org/10.1038/s41467-025-64187-3

Collectivity effect in cluster catalysis under operational conditions

Received: 27 May 2025

Accepted: 8 September 2025

Published online: 15 October 2025

Check for updates

Jia-Lan Chen[1], Xue-Chun Jiang[1], Li Feng[1], Jinze Zhu[1], Jian-Wen Zhao[1], Jin-Xun Liu[1,2] ✉ & Wei-Xue Li[1,2] ✉

Subnanometer metal clusters are promising catalysts but are limited by structural heterogeneity and dynamics under *operational* conditions. Herein, we employ artificial intelligence-enhanced multiscale modeling, integrated with statistical analysis, to exhaustively explore the catalytic sites of cluster catalysts under reaction conditions. We discover that numerous sites across varying sizes, compositions, isomers, and locations collectively contribute to overall activity due to their high intrinsic activity and abundance. The collectivity of active sites, despite their distinct local environments, configurations and reaction mechanisms, arises from their high intrinsic activity and considerable population. Data-driven machine learning reveals that this collectivity is governed by the balance between local atomic coordination and the adsorption energy. Using CO oxidation on Cu/CeO_2 as an example, we validate the collective effect via agreement between computed mechanisms/kinetics and experimental data. This work provides insights into active sites in heterogeneous catalysis and highlights the potential of leveraging collective effects in cluster catalysis.

The active sites of catalysts, first introduced by H. S. Taylor in 1925, are among the most important yet elusive concepts in heterogeneous catalysis[1–3]. For supported nanocatalysts, this implies a specific ensemble of atoms, which accommodate not only reactant adsorption but also elementary reaction steps and product desorption, thus enabling their application in various chemical reactions[4–6]. Despite extensive investigations thus far, pinpointing the exact location of these active sites at the atomic level and their specific contribution to the observed overall activity remains challenging[7]. This is due to the intrinsic heterogeneity of the nanocatalysts involved, a complex function of the particle size and morphology, which limits the corresponding activity and selectivity[8,9]. On the other hand, atomically dispersed catalysts offer complete atom utilization and high selectivity owing to their improved site homogeneity; however, their limited number of available sites, lower mass-specific activity, and long-term stability restrict their broad application[10,11]. However, supported subnanometer cluster catalysts (SCCs), which are composed of a small group of active metal atoms with better stability, possess multiple sites allowing complex chemical reactions but remain sufficiently small for high atom utilization and selectivity[12–17]. These unique properties have made SCCs promising alternatives, as evidenced by the increase in their applications in various catalytic reactions, such as hydrogenation processes[18–21], oxidation reactions[22,23], and many other chemical transformations[24–26].

To take advantage of SCCs, full exploration of the configuration space is essential but challenging[27], since more than thousands of distinct isomers and sites on each isomer due to their intricate permutations and combinations are involved. Moreover, SCCs frequently undergo significant dynamic transitions owing to the close energetics of various isomers and the potential agglomerations/decompositions of clusters of different sizes[28–30]. Finally, many undercoordinated atoms tend to interact strongly with reactants and/or intermediates, which significantly changes their chemical states and morphologies[31]. These small cluster catalysts are subject to dramatic structural,

[1]State Key Laboratory of Precision and Intelligent Chemistry, School of Chemistry and Materials Science, University of Science and Technology of China, Hefei, Anhui, China. [2]Hefei National Laboratory, University of Science and Technology of China, Hefei, China. ✉e-mail: jxliu86@ustc.edu.cn; wxli70@ustc.edu.cn

compositional, and size variations under *operational* conditions, which profoundly influence their catalytic activity, selectivity, and stability[32–36]. Although there is increasing consensus on the importance of metastable sites with low concentrations for overall reaction rates[37–40], identification of the very nature of SCCs with full resolution of cluster sizes, isomers, compositions, sites, and reaction pathways for rational design of atom-efficient catalysts remains a challenge.

Herein, we leveraged a machine learning-based multiscale framework to reveal unique catalysis by SCCs. Through the statistical investigation of isomers and the use of data-driven machine learning techniques, we demonstrate a collective effect across different cluster sizes, compositions, isomers, and exposed sites and their impact on reaction pathways and overall activity. Here, we investigated CO oxidation catalyzed by CeO_2(111)-supported Cu[41]. CO oxidation is selected for its simplicity, and extensive experimental data are available, which is perfect for developing corresponding foundational theories for SCCs. Cu is considered a viable alternative to the noble metals Pt, Pd, and Rh in three-way catalysts, and compared with other CeO_2 surfaces, CeO_2(111) has the highest activity for CO oxidation[42].

We discovered that Cu clusters are more active than single-atom and extended-surface catalysts. A variety of active sites, which are composed of different ensembles across various cluster sizes, compositions, isomers, and sites composing both Mars–van Krevelen (MvK) and Langmuir–Hinshelwood (LH) mechanisms, collectively contribute to activity. Using data-driven machine learning techniques, we identify key activity descriptors and uncover the principles governing collective catalytic behavior. Despite distinct reaction pathways and energy landscapes, the collectivity effect emerges from the synergy of high intrinsic activity, dictated by the local environment, and moderate reactant adsorption, coupled with a substantial population of active sites. By incorporating the statistical distribution of cluster isomers and active sites, we determined the key structural parameters, reaction rates, and activation barriers for the Cu/CeO_2(111) catalysts, which strongly agreed with the experimental data. This analysis offers crucial insights for catalyst design by optimizing the distribution and population of collective active sites within specific clusters, thereby significantly enhancing the overall catalytic performance.

Results

A machine learning-based framework for heterogeneous cluster catalysis

We leveraged a multiscale modeling and four-step strategy to pinpoint the nature of the active sites and corresponding reaction pathways for SCCs under *operational* conditions (Fig. 1). To determine the structure and composition of supported clusters under reaction conditions, we first conducted genetic algorithm (GA)-driven modified grand canonical Monte Carlo (M-GCMC) simulations, as detailed in the Supplementary Information and Supplementary Figs. 1–2. Artificial neural network potentials (ANNPs) were employed to accelerate the M-GCMC simulations, where more than 100,000 cluster structures were sampled. In this way, all possible structures of clusters of different sizes and isomers with the right adsorption and coverage of reactants and intermediates are identified. Considering their free energy of formation, the corresponding distributions and/or concentrations of all the clusters identified, including the metastable ones under thermodynamic equilibrium, are identified according to the Boltzmann distribution law. For practical synthesis, where thermodynamic equilibrium might not be necessarily reached, a cluster distribution from experiments, if available, could be applied.

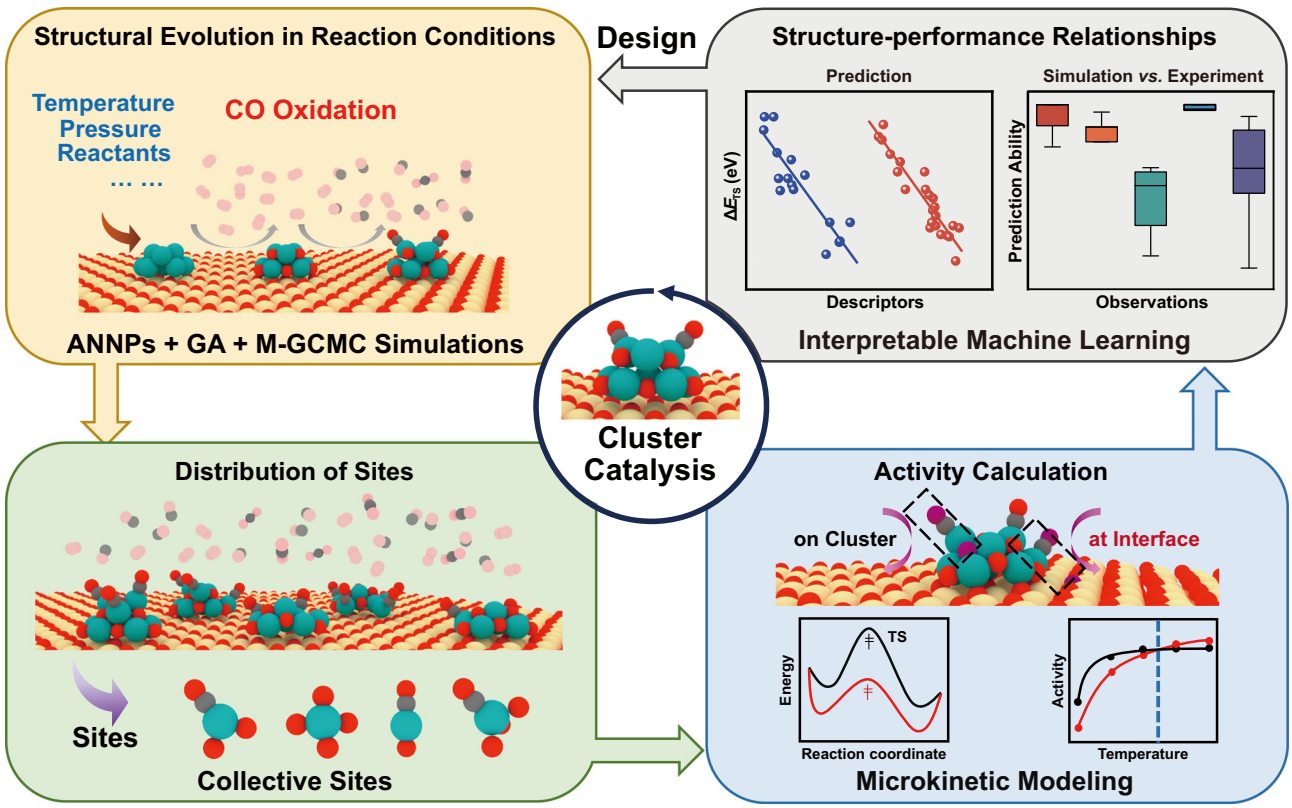

Fig. 1 | Workflow for studying cluster catalysis under reaction conditions. There are four parts: identifying the cluster catalyst composition and structure under *operational* reaction conditions via machine learning-accelerated grand canonical Monte Carlo (GCMC) simulations; assessing the statistical distributions of sites; computing the reaction rates for each site within the cluster via microkinetic modeling; and gaining a deeper understanding of the sites and comparisons between simulations and experiments. The red, yellow, green, and gray spheres are the O, Ce, Cu, and C atoms, respectively. This notation is used throughout the paper.

For each cluster isomer identified, we considered all exposed sites and optimized the corresponding reaction pathways, from which the isomer- and site-resolved intrinsic reaction rates were calculated via first-principles microkinetics. This process is repeated for all clusters in terms of different isomers and sizes in the presence of adsorbates. By integrating the intrinsic activity of all available sites, weighted by the appropriate distribution function, the overall catalytic activity can be quantified. Here, as a simplification, the sites with the same local coordination number and coordinated reactants/intermediates across all clusters are classified as one type of site. The resulting average reaction rate per site (R^o) of a cluster catalyst accounting for different cluster sizes, isomers, and sites is therefore determined by:

$$R^o = \sum_n p_n R_n = \sum_n p_n \left(\sum_{site} p_{n,site} \times r_{n,site} \right) \quad (1)$$

where p_n represents the population of clusters with n metal atoms and R_n denotes the average reaction rate per site for that cluster. $p_{n,site}$ and $r_{n,site}$ refer to the population and reaction rate of a specific site within an n-atom cluster. When isomer distributions are incorporated, R_n for a specific cluster size n is expressed as:

$$R_n = \sum_{iso} (P_{n,iso} \times R_{n,iso}) = \sum_{iso} \left[P_{n,iso} \times \left(\sum_{site} p_{n,iso,site} \times r_{n,iso,site} \right) \right] \quad (2)$$

where $R_{n,iso}$ denotes the average reaction rate per site for a specific isomer of an n-atom cluster, determined by its population $P_{n,iso}$ and site-specific contributions, which depend on the population of the site $p_{n,iso,site}$ and its corresponding reaction rate $r_{n,iso,site}$. The populations p_n, $P_{n,iso}$, $p_{n,site}$ and $p_{n,iso,site}$ are derived from Boltzmann distributions on the basis of Gibbs formation energy calculations, with the detailed methodology provided in Supplementary Note 1. This framework enables a comprehensive calculation of the reaction rate by summing contributions from all cluster sizes, compositions, isomers, and exposed sites, capturing the collective effects in cluster catalysis. Compared with those in experiments, the contributions from specific sites and/or isomers and their collective effects can be identified but are difficult to extract from experiments otherwise. Finally, we used an interpretable machine learning algorithm (SISSO)[43] to build a physically meaningful descriptor of activity in terms of the geometric and energy features, providing valuable guidance for the rational design of more efficient SCCs. **Structures and components of Cu_8/CeO_2 under *operational* conditions.**

We first studied CO oxidation on the "magic-numbered" Cu_8 cluster on CeO_2(111). Cu_8 is selected because it closes the first icosahedral shell (maximal intrinsic stability), and ~1 nm Cu_8 ensembles are routinely observed on CeO_2 under CO/O_2 feeds, making it the standard experimental benchmark for Cu/CeO_2 catalysis[42]. Note that, under the CO oxidation conditions considered ($T = 400$ K and $P_{CO} = P_{O2} = 0.02$ bar), we found that oxygen vacancies can be rapidly replenished either by O_2 dissociation or oxygen from the supported CuO_x clusters (Supplementary Figs. 3–4). Consequently, the presence of oxygen vacancies is excluded from the following M-GCMC simulations. The optimized clusters, denoted as $Cu_8(CO)_xO_y$, are shown schematically in Supplementary Figs. 5–8. As plotted specifically in Fig. 2a, when $\Delta\mu_{CO} < -1.23$ eV, no CO is adsorbed, and only dissociative oxygen atoms varying from four to eight adsorbs on Cu. However, when $\Delta\mu_{CO} > -1.23$ eV, CO starts to adsorb, varying from two to four. For CO and O_2 at partial pressures of 0.02 bar at 400 K ($\Delta\mu_{CO} = -0.86$ eV and $\Delta\mu_{O2} = -0.90$ eV, respectively)[44], the most stable structure identified is $Cu_8(CO)_2O_8$.

To quantify the contribution of meta-stable structures to overall activity, for safety, all metastable structures with a free formation energy difference of 0.50 eV were considered (Fig. 2b and Supplementary Fig. 9). In accordance with the Boltzmann statistical distribution law, this means that isomers with populations as low as ~10^{-7} at 400 K were included. The most stable and populated cluster identified was $Cu_8(CO)_2O_8$, with the highest population $P_{8,c,iso}$ of 47%. $Cu_8(CO)_3O_8$, with one more CO molecule, was also identified as a prominent cluster. It has two possible isomers, **α** and **β**, with corresponding populations of 17% and 4.2%, respectively (21.2% in total; details are provided in Supplementary Fig. 9 and Supplementary Table 1). The third cluster identified is $Cu_8(CO)_4O_8$ with one more CO, and it has three possible isomers, **α, β** and **γ**, with populations of 16%, 13%, and 2.1% (31.2% in total), respectively (Fig. 2b).

The isomers identified above exhibit a characteristic bilayer structure. Three high-lying Cu atoms bind preferentially to CO molecules and dissociative oxygen atoms, whereas five low-lying interfacial Cu atoms bind to the CeO_2 support in a pentagonal configuration. Across all the isomers identified, the exposed sites can be classified into four distinct interfacial sites (labeled $\mathbf{I_A}$ to $\mathbf{I_D}$) and three distinct on-cluster sites (labeled $\mathbf{O_A}$ to $\mathbf{O_C}$) (Fig. 2c, Supplementary Fig. 10 and Table 1). Specifically, the most prevalent isomer, $Cu_8(CO)_2O_8$, contains five interfacial sites (four $\mathbf{I_A}$s and one $\mathbf{I_B}$) and three on-cluster sites (one for each $\mathbf{O_A}$, $\mathbf{O_B}$, or $\mathbf{O_C}$) (Fig. 2d). However, for $Cu_8(CO)_3O_8$, the $\mathbf{O_A}$ site is no longer available for the more populated isomer **α**, and one $\mathbf{I_A}$ site is replaced by one $\mathbf{I_C}$ site for the less populated isomer **β**. For $Cu_8(CO)_4O_8$ with three isomers, the $\mathbf{I_A}$ sites remain the most populated, and the $\mathbf{O_A}$ site is available only for isomer **β**. In terms of the site distribution $p_{n,\ sites}$ across the Cu_8 clusters considered can be concluded that the interfacial sites are the most abundant, with an overall population of 64%, and the corresponding populations for the $\mathbf{I_A}$, $\mathbf{I_B}$, $\mathbf{I_C}$ and $\mathbf{I_D}$ sites are 40%, 14%, 9%, and 1%, respectively. The on-cluster sites $\mathbf{O_A}$, $\mathbf{O_B}$ and $\mathbf{O_C}$ had populations of 14%, 13%, and 9% (36% in total), respectively.

CO oxidation on the Cu_8/CeO_2 cluster catalysts

The optimized reaction pathway and potential energy surface (PES) for CO oxidation were identified for all classified sites. Here, both the Mars–van Krevelen (MvK) and Langmuir–Hinshelwood (LH) pathways were considered (Fig. 3a). Note that we also considered the Eley–Rideal (ER) pathway between the gas CO and dissociative oxygen atoms on the supported clusters. For the typical sites tested, the corresponding barriers were comparable to those of the LH pathways (Supplementary Table 2). Considering its much smaller prefactor, its contribution to the overall reactivity was not considered in the following study. Moreover, the participation of lattice oxygen via spillover to the supported Cu cluster for CO oxidation was also excluded because of its dramatically high diffusion barrier of 2.44 eV (Supplementary Fig. 11).

For the interface sites, the MvK pathway is preferred. The most populated $\mathbf{I_A}$ sites display the highest elementary barrier of 1.36 eV for CO reacting with lattice oxygen (Supplementary Figs. 12–13). The least populated $\mathbf{I_D}$ sites also have considerable barriers of 0.91 eV (Supplementary Figs. 14–17 and Supplementary Tables 3–4). The moderately populated $\mathbf{I_B}$ and $\mathbf{I_C}$ sites presented yet modest barriers of 0.58 and 0.72 eV, respectively (Fig. 3b, Supplementary Fig. 18 and Supplementary Table 3); therefore, these two sites would contribute more to the overall activity. Note that CO oxidation via the nondissociative O_2 pathway is also preferable because of its rather small barrier of ~0.04 eV. Compared with the MvK pathway, benchmark calculations revealed that the LH reaction pathway has a much higher elementary barrier of 0.18 eV at the interface sites (Supplementary Table 2).

However, for the on-cluster sites, the LH pathway is favorable. The calculated PES values indicate that the reaction prefers to occur at the $\mathbf{O_A}$ site with the highest elementary barrier of 0.74 eV only (Fig. 2c and Supplementary Fig. 19). Here, the optimized reaction pathway reveals that CO reacts with an O atom from the dissociative adsorption of O_2, whereas direct CO oxidation via molecular O_2, known as the bifunctional effect, encounters a barrier of 0.68 eV greater. The less populated $\mathbf{O_B}$ and $\mathbf{O_C}$ sites have barriers higher than 1.23 eV (Supplementary

https://doi.org/10.1038/s41467-025-64187-3

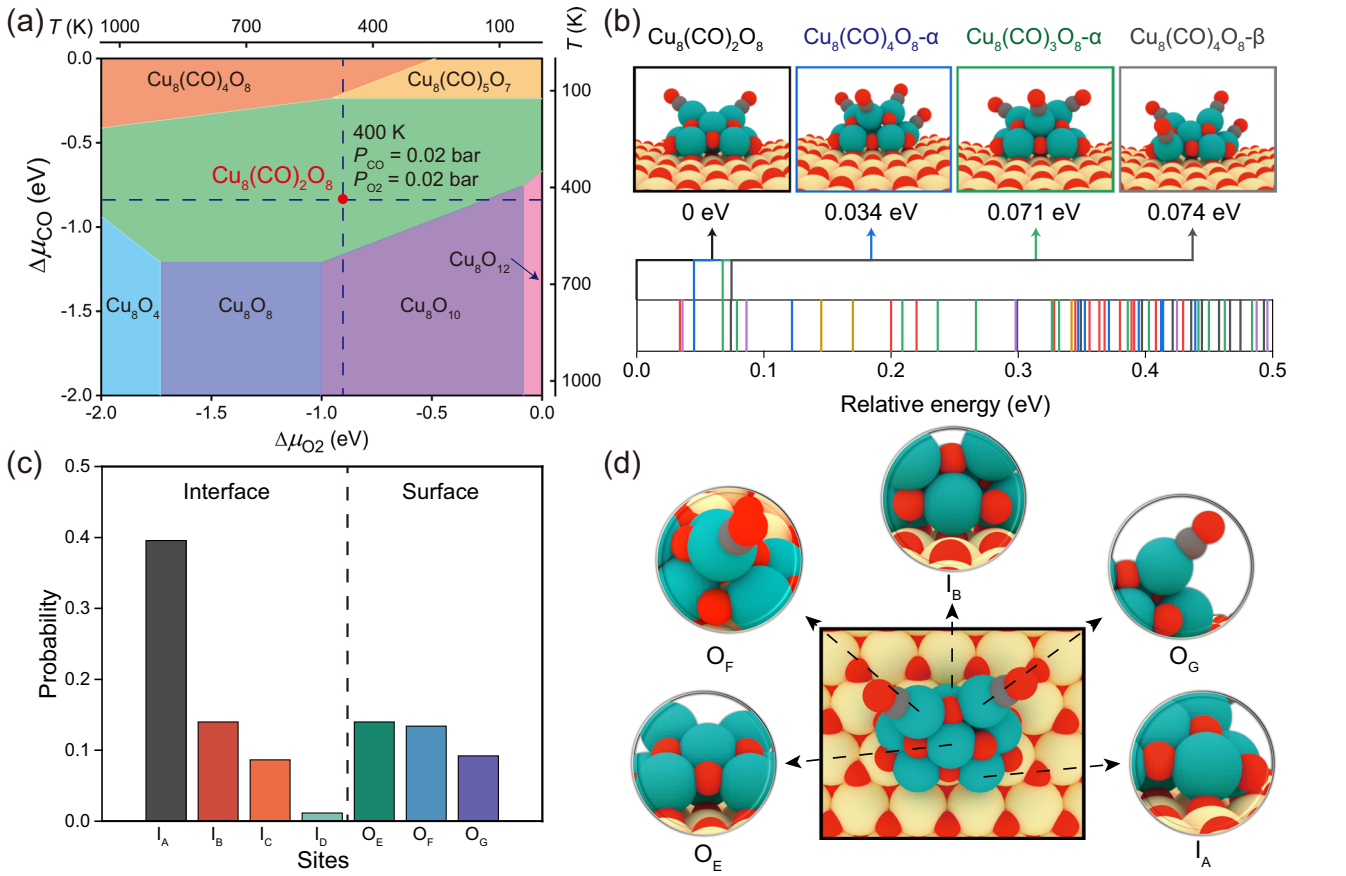

Fig. 2 | Identification of the structures and compositions of the Cu_8/CeO_2 cluster catalysts under operational conditions. a Phase diagram of Cu_8 cluster catalysts as a function of the chemical potentials of gaseous CO and O_2. **b** Isomers of the $Cu_8(CO)_xO_y$ clusters within a 0.50 eV energy window at 400 K, considering CO and O_2 partial pressures of 0.02 bar. **c** Probability distribution of sites with probabilities exceeding 1% in the $Cu_8(CO)_xO_y$ metastable ensemble structure pool on the basis of the proximity of Cu atoms within a cutoff radius of 1.15 times the standard bond length. **d** Five different sites of the most stable $Cu_8(CO)_2O_8$ structure under typical CO oxidation conditions ($T = 400$ K and $P_{CO} = P_{O2} = 0.02$ bar).

Figs. 20–23 and Supplementary Tables 3–4). This makes the $\mathbf{O_A}$ sites among the on-cluster sites the most likely contributors to the overall activity. The intrinsic reaction rates of seven classified sites, $r_{8,site}$, were calculated via microkinetic modeling on the basis of optimized PESs (Fig. 3d and Supplementary Table 5). The $\mathbf{I_C}$ and $\mathbf{O_A}$ sites had the highest $r_{8,site}$ values of 9.6×10^{-2} and 6.0×10^{-2} s^{-1}, respectively, because their lowest apparent barrier E_{app} values were 0.22 eV and 0.12 eV, respectively. The $\mathbf{I_D}$ sites exhibit a lower $r_{8,site}$ of 6.6×10^{-3} s^{-1} because of their slightly higher E_{app} (0.32 eV). Notably, although the $\mathbf{I_B}$ sites had a similar apparent E_{app} of 0.37 eV, the calculated $r_{8,site}$ was 3.1×10^{-5} s^{-1}, two orders of magnitude lower because their oxygen coverage was three orders of magnitude lower than that of the $\mathbf{I_C}$ and $\mathbf{O_A}$ sites (Supplementary Fig. 24). However, the $\mathbf{I_A}$, $\mathbf{O_B}$, **and** $\mathbf{O_C}$ sites had the lowest $r_{8,site}$ of 8.2×10^{-6} s^{-1} because of their considerable E_{app} of at least 0.77 eV.

The $\mathbf{I_C}$ and $\mathbf{O_A}$ sites had the highest $r_{8,site}$ and considerable population p_{site} values (8.6% and 14%), and the corresponding effective rates R_8 were the highest at 8.2×10^{-3} and 8.3×10^{-3} s^{-1}, respectively (Fig. 3e). For the $\mathbf{I_B}$ sites, although their $p_{8,site}$ is considerable, their three orders of magnitude smaller $r_{8,site}$ results in a much smaller R_8 (4.3×10^{-5} s^{-1}). For the $\mathbf{I_D}$ sites, since both $p_{8,site}$ and $r_{8,site}$ are small, the corresponding R_8 values are smaller as well, which are actually very close to those of the $\mathbf{I_B}$ sites. For the $\mathbf{I_A}$, $\mathbf{O_B}$, **and** $\mathbf{O_C}$ sites, their $r_{8,site}$ values are further decreased by at least 5 orders of magnitude. As a result, both the interfacial $\mathbf{I_C}$ sites via the MvK pathway and the on-surface $\mathbf{O_A}$ sites via the LH pathway determine and contribute roughly equally to the overall reaction rate. This reveals a collective effect on how the individual sites contribute distinctly to the overall reactivity.

Although the site-resolved activity is insightful from an atomic point of view, the isomer-resolved activity $R_{8,iso}$ provides another constructive view for rational design. In this context, the site-resolved activity derived was used as input for the specific isomer considered (Supplementary Table 6). $Cu_8(CO)_2O_8$ has the highest population $p_{8,iso}$ of 47% and contains one active $\mathbf{O_A}$ site, and the corresponding reaction rate $R_{8,iso}$ is considerable at 3.5×10^{-3} s^{-1}. For $Cu_8(CO)_3O_8$, the **β** isomer contains one active $\mathbf{I_C}$ site, but its $p_{8,iso}$ (4.2%) is rather low, resulting in a relatively small $R_{8,iso}$ of 8.4×10^{-4} s^{-1}. For $Cu_8(CO)_4O_8$, the **α** and **β** isomers have high $p_{8,iso}$ values of 17% and 13%, respectively, and both contain one active $\mathbf{O_A}$ site; the resulting $R_{8,iso}$ values are considerable at 2.1×10^{-3} s^{-1} and 2.6×10^{-3} s^{-1}, respectively. For the remaining isomers of $Cu_8(CO)_3O_8$-**α** and $Cu_8(CO)_4O_8$-**γ**, the corresponding reaction rates can be neglected because of the absence of active sites and/or the lower $p_{8,iso\ values}$, respectively. Therefore, the isomer-resolved reaction rates $R_{8,iso}$ for $Cu_8(CO)_4O_8$, $Cu_8(CO)_2O_8$, and $Cu_8(CO)_3O_8$ are 4.7×10^{-3}, 3.5×10^{-3} and 8.4×10^{-4} s^{-1}, respectively. In addition to configurational isomers of a given stoichiometry, clusters of different stoichiometries are also populated, and the combined ensemble of these species collectively shapes the observed reactivity.

Size effect of the Cu/CeO_2 cluster catalysts

We further explored the impact of cluster size by considering Cu_m clusters (m = 1–4) to account for dynamic transformations and size

https://doi.org/10.1038/s41467-025-64187-3

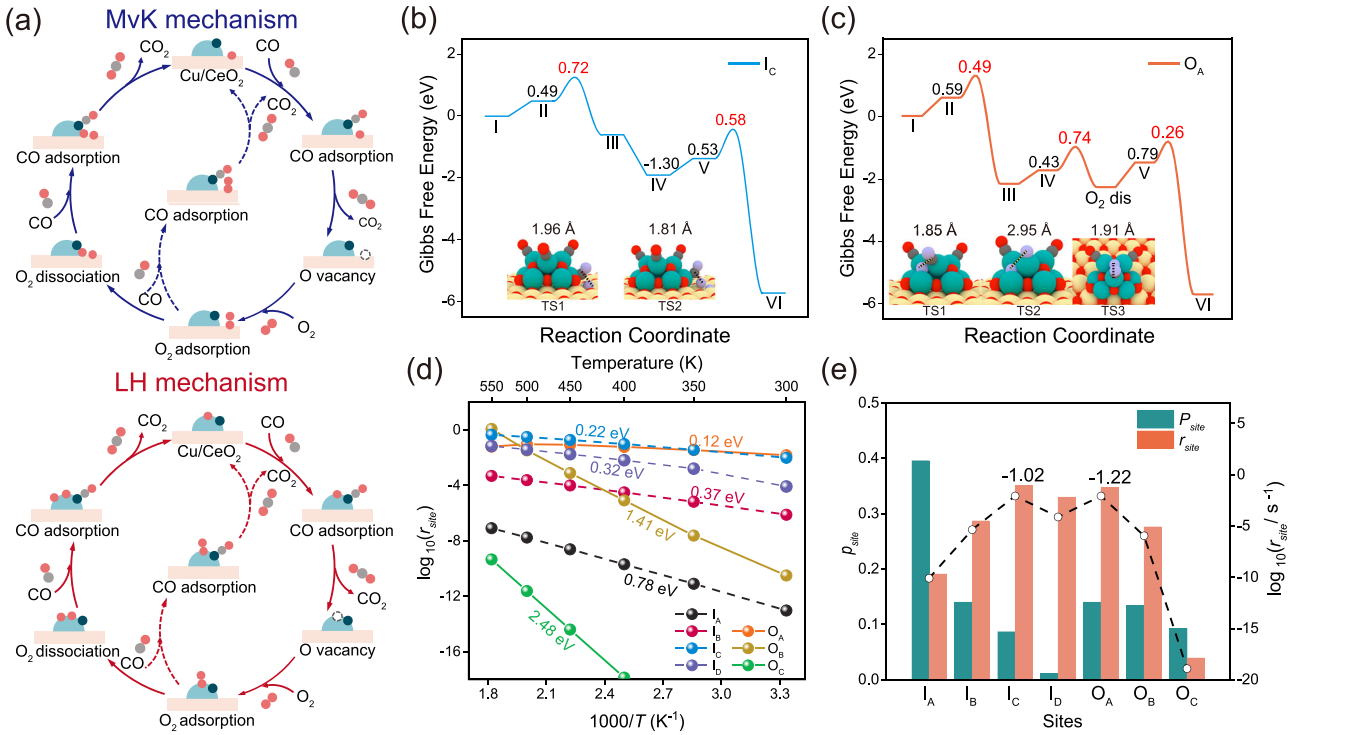

Fig. 3 | Study of the CO oxidation mechanism over the Cu_8/CeO_2 cluster catalyst. a Pathways illustrating the interface reaction mechanism and cluster surface reaction mechanism in cluster catalysts during CO oxidation. The solid and dotted lines represent the dissociation and nondissociation pathways, respectively. The dark blue point, red point, and gray spheres indicate the Cu atom, O atom, and C atom, respectively. The white spheres are oxygen vacancies. We used the oxygen atoms in the $CuO_x(CO)_y/CeO_2$ clusters to initiate CO oxidation. **b** The most favorable pathway among the interface reactions. The purple spheres are O atoms involved in CO oxidation. **c** The most favorable pathway among cluster surface reactions. **d** CO_2 formation rates (r_{site}) at different temperatures for each site in the $Cu_8(CO)_xO_y/CeO_2$ cluster catalyst, as determined via microkinetic modeling. The apparent activation barriers are indicated in eV. **e** Distribution of the probability of sites and corresponding CO_2 formation rates.

heterogeneity in the as-prepared catalysts. The most stable structure of the Cu_m clusters, along with favorable adsorbate coverage, was identified via M-GCMC simulations at 400 K under 0.02 bar CO and 0.02 bar O_2 (Supplementary Figs. 25–38). To assess their relative stability, a CuO nanoparticle (NP) with a curvature radius of 1.5 nm was used as a zero-energy reference, as Cu tends to oxidize under oxygen-rich conditions. The chemical potential of the CuO NPs was calculated via the Gibbs–Thomson equation, $\Delta\mu = 2\Omega\gamma/R$, where γ was approximated by the effective surface energy from the Wulff construction of bulk CuO[45,46] under the same conditions (Supplementary Figs. 31, 39–45). ANNP calculations revealed that Cu_3O_4 and $Cu_8(CO)_2O_8$ are approximately 0.30 eV less stable per Cu atom than bulk CuO/Cu_2O is but 0.32 eV more stable than metallic Cu at 400 K and $P_{CO} = P_{O2} = 0.02$ bar (Supplementary Table 7). However, detaching a single Cu requires >2 eV (Supplementary Fig. 46), so oxidic subnm ensembles remain thermodynamically preferred and kinetically trapped, matching operando XAFS/XPS observations of persistent Cu oxide clusters on CeO_2[42].

The most stable Cu_3 and Cu_8 clusters identified had exothermic formation free energies of −0.17 and −0.18 eV/Cu atom, respectively. Specifically, the Cu_3 cluster binds to the CeO_2 support in a favorable triangular configuration, whereas Cu_4 exhibits a quadrilateral configuration with a thermally neutral formation free energy. In contrast, Cu_1 and Cu_2 have endothermic formation energies of 0.96 eV/Cu atom and 0.14 eV/Cu atom, respectively, making them unfavorable and prone to agglomeration (Fig. 4a and Supplementary Fig. 45). MD simulations (1 ns, 400 K) by ANNPs show that $Cu_8(CO)_2O_8/CeO_2(111)$ remains intact with no Cu detachment (Supplementary Fig. 47). The most accessible breakup, $Cu_8 \rightarrow Cu_7 + Cu_1$, is uphill by $\Delta G = 1.33$ eV and traverses a 2.06 eV barrier (Supplementary Fig. 46); all other channels ($Cu_6 + Cu_2$, $Cu_5 + Cu_3$, and $Cu_4 + Cu_4$) are > 1.98 eV endergonic (Supplementary Fig. 47). Such energetics render such events negligible under *operational* conditions. Therefore, Cu_3, Cu_4 and Cu_8 clusters can coexist under *operational* conditions, although Cu_4 has a lower population. The equilibrium concentrations of these clusters were determined on the basis of their energetics, with Cu_3, Cu_4 and Cu_8 as the predominant species, corresponding to monolayer coverages of 0.078, 4.8×10^{-3} and 0.175 ML, respectively (Supplementary Formula S31 and Supplementary Table 8). The coverage for other species was negligible. On the basis of these coverages, the total Cu loading on $CeO_2(111)$ was calculated to be 6.9%, which agrees well with the experimental data[42,44,47,48] (Supplementary Table 8). Although direct experimental visualization of smaller cluster species remains challenging, our approach effectively elucidates their catalytic contributions to diverse cluster sizes, compositions, isomers, sites and mechanisms (Fig. 4b and Supplementary Figs. 48–70), complementing experimental findings. We observed a decrease in R_n with decreasing cluster size. For small clusters (those with fewer than 3 atoms), the isomer and site types are unique, with R_n determined solely by the $r_{n,site}$. For Cu_4 and CuO(111), there are 3 and 2 different types of sites, respectively (Supplementary Tables 9–12). The interfacial $\mathbf{I_A}$ sites on Cu_4 and CuO have the highest $r_{n,site}$ values of 7.9×10^{-3} and 7.3×10^{-2} s^{-1}, accounting for 48.6% and 50% of all available sites, respectively (Supplementary Table 9). In Cu_3, only one $\mathbf{O_A}$ site has a $r_{n,site}$ value of 5.4×10^{-3} s^{-1}, whereas the other sites have $r_{n,site}$ values of less than 10^{-5} s^{-1}, rendering their contribution to the overall conversion rates negligible. As a result, the Cu_8 cluster and CuO(111) surface exhibit the highest R_n values, achieving rates of approximately 10^{-2} s^{-1} and the lowest E_{app} values of 0.19 eV and 0.11 eV, respectively. Smaller clusters such as Cu_3 and Cu_4 have slightly lower R_n values (~10^{-3} s^{-1}) and higher E_{app} values

https://doi.org/10.1038/s41467-025-64187-3

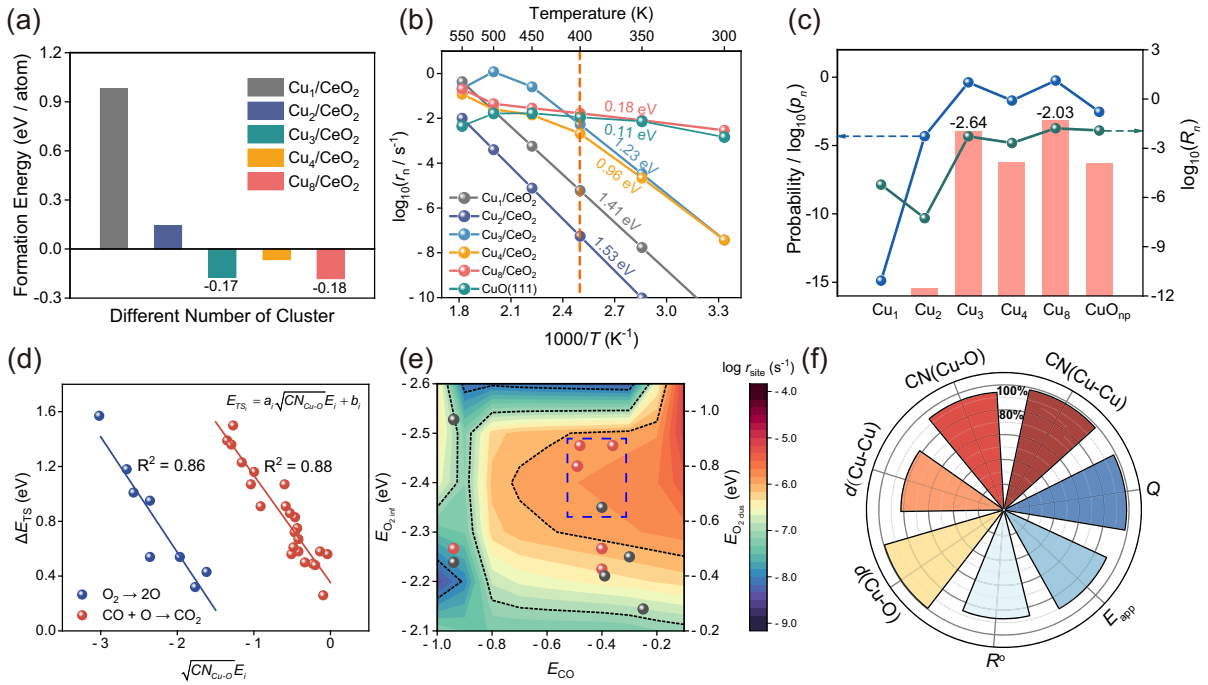

Fig. 4 | Effect of the Cu cluster size on CO oxidation. a The calculated formation energies of the $Cu_m(CO)_xO_y$ clusters on the $CeO_2(111)$ surface with respect to the 3 nm CuO nanoparticles at 400 K with CO and O_2 partial pressures of 0.02 bar. **b** CO_2 formation rates of the Cu clusters (r_n) predicted via microkinetic modeling. The apparent activation barriers are indicated in eV. The reaction rates at 400 K are given for different Cu clusters. **c** The distribution probabilities (blue plot), CO oxidation rates (r_n) (green plot), and total CO conversion rates of Cu clusters of different sizes (R_n) (orange column). **d** The correlation between the transition state energies for O_2 dissociation and CO oxidation and the adsorption energy of O_2 (depicted in blue) or CO (depicted in red) across various Cu/CeO_2 sites on the basis of interpretable machine learning. **e** Activity map illustrating the relationship between the reaction rate of sites (r_{site}) and the adsorption energies of CO and O_2 at different sites on the Cu/CeO_2 cluster catalyst, which vary in size. The red and gray points represent the sites on the cluster surface or at the interface, respectively. **f** Deviations between the simulations and experiments for 7 observations, namely, *CN*(Cu-Cu), *CN*(Cu-O), *d*(Cu-Cu), *d*(Cu-O), R^o, E_{app} and *Q*.

(0.96–1.22 eV). In contrast, the smallest units—Cu_1 single atoms and Cu_2 dimers—display the lowest activity, with rates of 6.0×10^{-6} s^{-1} and 5.5×10^{-8} s^{-1}, respectively, and E_{app} values exceeding 1.41 eV.

The high R_n values of the Cu_3 and Cu_8 clusters arise from their large populations (41.8% and 56.0%) and the presence of key active sites—on-surface $\mathbf{O_A}$ for the Cu_3 and $\mathbf{I_C}$ sites and on-surface $\mathbf{O_A}$ sites on Cu_8 (Fig. 4c). These sites collectively enhance CO oxidation activity. In contrast, less stable structures, such as the Cu_1 single atom, Cu_2 dimer, Cu_4 cluster, and CuO(111) surfaces, make minimal contributions because of their lower intrinsic activity and/or fewer exposed sites. For example, Cu_4 and CuO have low distributions (1.9% and 0.28%, respectively) (Supplementary Table 8), leading to R_n values of 4.0×10^{-5} s^{-1} and 3.5×10^{-5} s^{-1}, respectively. Cu_1 and Cu_2, with even lower distributions (1.3×10^{-15} and 4.8×10^{-5}), display significantly low conversion rates of 7.9×10^{-21} and 2.6×10^{-12} s^{-1}, respectively.

Our calculation results suggest that Cu_3 or Cu_8 clusters are optimal for enhancing the catalytic efficiency and stability. The precise synthesis of these clusters, followed by deposition on CeO_2 supports, is critical for maximizing CO oxidation activity, even when the cluster exhibits significant dynamic variation among metastable isomers. Furthermore, our analysis revealed that 68.2% of the activity arises from LH mechanisms, whereas 31.8% is driven by MvK mechanisms, accounting for the population of both interface and surface sites. Despite the different pathways, both mechanisms exhibit similar activation barriers (~0.70 eV) for the rate-determining step of CO reacting with atomic O. These findings highlight another mechanistic collectivity of Cu/CeO_2 systems.

To uncover the origin of collectivity in cluster catalysis, we identified key descriptors linking transition state energies for CO oxidation across clusters of varying sizes and the CuO(111) surface via data-driven compressed sensing analysis (Supplementary Note 3). Our analysis revealed that the transition state energies for CO oxidation and/or O_2 dissociation are significantly influenced by factors such as E_{CO}, E_{O2}, and Cu–O coordination number ($CN_{Cu\text{-}O}$) within both the cluster and support (Fig. 4d). By applying the derived equation for transition state energy estimation in microkinetic simulations, we constructed a two-dimensional activity map that illustrates how varying CO and O_2 adsorption energies affect r_{site} (Fig. 4e).

The collectivity effect arises from the local environment of the Cu sites, captured by the Cu–O binding energy coordination number ($BECN_{Cu\text{-}O}$) descriptor and the adsorption energies of CO and O_2 (E_i). $BECN_{Cu\text{-}O}$ is a key factor linking geometric and mechanistic aspects to catalytic performance (Supplementary Note 3). It serves as a crucial descriptor for determining the activation barriers and reaction rates in CO oxidation (Supplementary Fig. 71). The Cu–O coordination number ($CN_{Cu\text{-}O}$), CuO formation energy, and $CeO_2(111)$ vacancy formation energy ($E_{M\text{-}O}$) collectively influence the transition state energy, directly impacting the catalytic activity.

As the cluster size increases, the reaction mechanism shifts from being primarily cluster-centered to surface and interface-driven

pathways. Specifically, as the cluster size increases from Cu_1 to Cu_4, the bond strength between Cu and CO weakens (from −1.87 eV to −0.45 eV, Supplementary Fig. 72), which lowers the CO oxidation barrier and increases the CO oxidation rate. At larger sizes, such as Cu_8, the interface sites present lower $BECN_{Cu\text{-}O}$ values due to stronger $E_{M\text{-}O}$ in CeO_2 than in CuO, decreasing the activation barriers and increasing the reaction rates. These sites balance CO/O_2 adsorption and Cu−O bond strength, harmonizing the energy landscape and enhancing the mechanistic collectivity effect.

We found that collective active sites on stable Cu_3 and Cu_8 clusters, despite differing chemical environments and configurations, share similar intrinsic activities, contributing synergistically to the overall catalytic performance. In contrast, smaller species such as Cu_1 and Cu_2 have lower reactivities due to diminished surface coverage or higher energy barriers. However, Cu_1 and Cu_2 can migrate into CeO_2 lattice vacancies during catalyst preparation[49,50], forming bulk-like structures and potentially altering catalytic behavior (Supplementary Figs. 73–76). Our study shows that Cu_1 and Cu_2 doped into CeO_2 (111) exhibit activity rates of 4.4×10^{-16} and 6.5×10^{-3} s^{-1}, respectively. While the activity and activation energy (E_{app} of 1.19 eV) of $Cu_2Ce_{1\text{-}x}O_2(111)$ are comparable to those of Cu_3, this structure also contributes collectively to CO oxidation activity, similar to those of Cu_3 and Cu_8. The synthesis of such solid solution structures further enhances the CO oxidation performance, illustrating an additional collective effect in Cu/CeO_2 catalysis.

Discussion

We calculated key macroscopic observables for CO oxidation over Cu/CeO_2 catalysts for direct comparison with experimental data, with a focus on the CeO_2(111) surface. Future work will extend these studies to explore the catalytic properties of the (110) and (100) facets to understand facet-specific effects. The key parameters, including the Cu−O and Cu−Cu bond lengths (d(Cu–O) and d(Cu–Cu)), average coordination number (CN), Cu charge state (Q), overall reaction rate (R^o), and $E_{app,}$ were calculated (Supplementary Figs. 77–80 and Supplementary Table 13). For the Cu/CeO_2 system, the average d(Cu–O) was 1.92 Å, with a CN of 3.55 and a Q of approximately +0.98. The calculated reaction rate for CO oxidation was 0.011 s^{-1}, corresponding to 1.72×10^{-6} mol_{CO} g_{cat}^{-1} s^{-1} for catalysts with 1% Cu loading and an E_{app} of 0.63 eV.

Although we focused on equilibrium distributions, our study also considered deviations to better capture catalytic activity across varying cluster sizes and reaction environments. Cu loading and cluster size significantly influenced E_{app}, which decreased from ~1.22 eV (dominated by Cu_3) to ~0.18 eV (dominated by Cu_8). This correlates with an increase in the reaction rate from 10^{-4} s^{-1} to 10^{-2} s^{-1} as the Cu_3 and Cu_8 concentrations increase, whereas their depletion drastically reduces the activity (Supplementary Fig. 81). The experimentally measured E_{app} values (0.58–0.77 eV) align well with our simulations for systems containing both Cu_3 and Cu_8 clusters. In contrast, theoretical models based on a single most stable structure, such as $Cu_8(CO)_2O_8$, underestimate E_{app} for CO oxidation, whereas Cu_3O_4 overestimates it. Both structures lack the MvK reaction mechanism, which highlights the importance of collective structures across different cluster sizes. This insight advances our understanding of the mechanistic collectivity in CO oxidation, where both cluster and interface reactions are important. These findings help explain discrepancies in experiments that suggest either a cluster surface[42,44] or an interface reaction mechanism[48,51–53], depending on the distribution of Cu species and the reaction conditions. The results of the reaction mechanism calculations revealed two concurrent redox cycles—$Cu^+ \rightleftharpoons Cu^{2+}$ triggered by surface CO/O_2 activation and $Ce^{4+} \rightleftharpoons Ce^{3+}$ driven by lattice–oxygen exchange at the interface (Supplementary Figs. 79–80 and Supplementary Table 14)—in quantitative agreement with the experimental results[41,42,44].

Direct experimental identification of the collectivity effect and site distribution under operating conditions remains a significant challenge owing to the transient nature of metastable isomers and the dynamic evolution of clusters in heterogeneous catalysis. In contrast, the introduced first-principles microkinetics-based statistical strategy provides a robust approach to address these challenges, offering a systematic and predictive understanding of cluster catalysis beyond the limitations of direct experimental observation. By considering the statistical distributions of isomers and active sites, our models align better with the experimental data, with the measured values for CN(Cu-Cu), CN(Cu-O), d(Cu-O) and d(Cu-Cu) closely matching the theoretical results, with deviations of less than 10%, except for the Cu–Cu bond length, which deviates by less than 20% (Fig. 4f and Supplementary Table 15)[42,44,48,51–57]. The agreement between the theoretical and experimental results emphasizes the robustness of the collective active sites in Cu/CeO_2 systems, providing a solid foundation for optimizing catalysts. We propose that synthesizing Cu_3 and Cu_8 clusters on CeO_2(111) through mass-selected cluster deposition or atomic layer deposition enhances CO oxidation activity, with further improvements possible by incorporating Ce vacancy sites with Cu_2 clusters. Our work challenges the traditional focus on single, well-defined cluster sizes, instead promoting catalyst designs that leverage the collective effects of multiple cluster sizes, isomers, and sites for more robust catalytic performance under realistic conditions.

In summary, by developing a machine learning-enhanced statistical and multiscale simulation framework, we revealed a collective effect of active sites across the surface and interface ensembles over various cluster sizes, compositions, and isomers on the overall activity of supported subnanometer cluster catalysts. This framework encompasses structure distribution under *operational* reaction conditions, statistical site analysis, pathway calculations, microkinetic modeling, and the development of descriptive models, providing an in-depth scenario with full details that moves beyond traditional approaches. Taking the Cu/CeO_2 system as an example, our study demonstrates that the collective behavior of numerous sites across various sizes, compositions and isomers drives CO oxidation, offering a comprehensive and holistic understanding of the catalytic process. The origin of the collectivity of the sites stems from their substantial intrinsic activity and the population of each individual site. Theoretical predictions from our framework have been validated against experimental data from mechanical, structural and kinetic points of view, reinforcing the robustness of our approach. This work not only deepens our understanding of the structural dynamics of supported cluster catalysts but also redefines the concept of active sites in heterogeneous catalysis, paving the way for the design of more efficient catalytic systems.

Methods

DFT calculations

All spin-polarized DFT calculations were performed via the Vienna Ab Initio Simulation Package (VASP 5.4.1) code[58]. The projector augmented wave (PAW)[59] pseudopotentials and the Perdew–Burk–Eznzerhof (PBE) exchange correlation functionals[60] were adopted. The Brillouin zone sampling was restricted to the Γ point with a $1 \times 1 \times 1$ mesh and a Monkhorst-Pack[61] $2 \times 2 \times 1$ mesh. An energy cutoff of 400 eV was used in the structure optimization. The geometric structure convergence threshold was set to 10^{-4} eV, with the optimization considered to have converged when the forces on each atom were less than 0.05 eV/Å. To account for the electron localization in the Ce 4f orbitals, the DFT + U method with U_{eff} = 5 eV[62] was employed.

Two O-Ce-O layers were employed for determining the structures and potential energy surfaces, with relaxation applied to the topmost O-Ce-O layer. A $p(4 \times 4)$ CeO_2(111) surface cell was employed. In addition, in CuO surface systems, there are three O–Cu–O layers on the

Cu_2O and CuO surface structures, with the topmost layer relaxed. For the CuO and Cu_2O systems, a $p(2 \times 2)$ supercell configuration was employed. A 15 Å vacuum spacing between adjacent slabs was used to avoid self-interaction. In this study, the strong correlation between Cu and O in the Cu/CeO_2 catalyst was disregarded, given that the effective U_{eff} value of 6.52 eV[63] used for the representative Cu_3O_4/CeO_2 and CuO(111) surface calculations does not influence our conclusions regarding the diagram and activity trend (Supplementary Figs. 82–86). Benchmark calculations indicate that varying the U value for Cu does not influence the trends in stability for the most stable or metastable structures of the representative Cu_3O_x/CeO_2 system (Supplementary Table 16), confirming the robustness of our stability assessments. Consequently, the U value for Cu was omitted in all the Cu cluster calculations. ANNPs have been rigorously tested and validated for Cu/CeO_2 systems across a range of cluster sizes, resulting in errors of less than 4 meV/atom, ensuring the reliability and consistency of the predicted energies, structural parameters, and magnetic states (Supplementary Table 17). All the structures obtained through the ANNP search process were subsequently verified via DFT calculations for accuracy.

Transition states were identified with the automated nudged elastic band method[64] and dynamic nudged elastic band method (dyneb)[65] to produce a good initial guess via the image-dependent pair potential (IDPP) surface method[66] to locate transition states with ANNPs as initial structures and identified with a force tolerance of 0.05 eV/Å via multiple methods, including the climbing image nudged elastic band (CI-NEB) method[67], improved dimer method[68,69], and force reversal method[70]. Vibrational mode analysis was also conducted to validate the identified transition states.

Ab initio molecular dynamics (AIMD) simulations were performed to calculate the radial distribution function (RDF) of different sizes of Cu clusters supported on CeO_2. The Nose–Hoover thermostat[71] was employed for NVT ensemble sampling at 400 K given the short physical duration of 10 ps in the AIMD simulations.

Bader charge analysis[72], as implemented by the Henkelman group, was performed. The electronic analysis of the crystal orbital Hamilton populations (COHPs)[73,74] was conducted by LOBSTER. Furthermore, the relationship between the transition state energies and the molecule adsorption energies was obtained via Sure Independence Screening and Sparsifying Operator (SISSO)[43].

The framework

The framework employs a multiscale simulation approach that combines embedded atom neural network (EANN) potentials[75] trained via active learning on a dataset generated via grand canonical Monte Carlo (GCMC) and ab initio molecular dynamics (AIMD) simulations to accurately and efficiently model the complex potential energy surfaces of Cu/CeO_2 catalysts. Genetic algorithm (GA) was used for global structure optimization, whereas modified GCMC (M-GCMC) simulations were applied to identify metastable structures under reaction conditions. Finally, microkinetic modeling was used to simulate the CO oxidation reaction kinetics and determine the apparent activation energies and dominant reaction mechanisms.

More details of the framework methods, such as ANNPs, the GA, GCMC simulations, and microkinetic modeling, can be found in the Supplementary Information.

Data availability

All calculation methods and data generated and analyzed during the study are provided in the Supplementary Information (SI) or can be obtained from the corresponding authors upon request. Source Data is provided with the manuscript. Data are available from the corresponding authors upon request. Source data are provided with this paper.

Code availability

The code developed in this work is available at the GitHub page https://github.com/chen-jialan/Collectivity-of-Cluster[76].

References

1. Zambelli, T., Wintterlin, J., Trost, J. & Ertl, G. Identification of the" active sites" of a surface-catalyzed reaction. *Science* **273**, 1688–1690 (1996).
2. Taylor, H. S. A theory of the catalytic surface. *Proc. R. Soc. Lond. Ser. A* **108**, 105–111 (1925).
3. Vogt, C. & Weckhuysen, B. M. The concept of active site in heterogeneous catalysis. *Nat. Rev. Chem.* **6**, 89–111 (2022).
4. Guo, Y., Wang, M. L., Zhu, Q. J., Xiao, D. Q. & Ma, D. Ensemble effect for single-atom, small cluster and nanoparticle catalysts. *Nat. Catal.* **5**, 968–968 (2022).
5. Liu, L. C. & Corma, A. Metal catalysts for heterogeneous catalysis: From single atoms to nanoclusters and nanoparticles. *Chem. Rev.* **118**, 4981–5079 (2018).
6. Cao, S., Tao, F. F., Tang, Y., Li, Y. & Yu, J. Size-and shape-dependent catalytic performances of oxidation and reduction reactions on nanocatalysts. *Chem. Soc. Rev.* **45**, 4747–4765 (2016).
7. Liu, L. C. & Corma, A. Evolution of isolated atoms and clusters in catalysis. *Trends Chem.* **2**, 383–400 (2020).
8. Cheng, H.-W. et al. Insights into heterogeneous catalysts under reaction conditions by in situ/operando electron microscopy. *Adv. Energy Mater.* **12**, 2202097 (2022).
9. Mou, T. Y. et al. Bridging the complexity gap in computational heterogeneous catalysis with machine learning. *Nat. Catal.* **6**, 122–136 (2023).
10. Yang, X.-F. et al. Single-atom catalysts: A new frontier in heterogeneous catalysis. *Acc. Chem. Res.* **46**, 1740–1748 (2013).
11. Wang, A., Li, J. & Zhang, T. Heterogeneous single-atom catalysis. *Nat. Rev. Chem.* **2**, 65–81 (2018).
12. Tyo, E. C. & Vajda, S. Catalysis by clusters with precise numbers of atoms. *Nat. Nanotechnol.* **10**, 577–588 (2015).
13. Rong, H., Ji, S., Zhang, J., Wang, D. & Li, Y. Synthetic strategies of supported atomic clusters for heterogeneous catalysis. *Nat. Commun.* **11**, 5884 (2020).
14. Xu, Z. et al. Size-dependent catalytic activity of supported metal clusters. *Nature* **372**, 346–348 (1994).
15. Li, X. et al. Advances in heterogeneous single-cluster catalysis. *Nat. Rev. Chem.* **7**, 754–767 (2023).
16. Liu, L. & Corma, A. Confining isolated atoms and clusters in crystalline porous materials for catalysis. *Nat. Rev. Mater.* **6**, 244–263 (2021).
17. Sun, L., Reddu, V. & Wang, X. Multiatom cluster catalysts for efficient electrocatalysis. *Chem. Soc. Rev.* **51**, 8923–8956 (2022).
18. Dong, C. et al. Fully exposed palladium cluster catalysts enable hydrogen production from nitrogen heterocycles. *Nat. Catal.* **5**, 485–493 (2022).
19. Gu, J. et al. Synergizing metal–support interactions and spatial confinement boosts dynamics of atomic nickel for hydrogenations. *Nat. Nanotechnol.* **16**, 1141–1149 (2021).
20. Crampton, A. S. et al. Structure sensitivity in the nonscalable regime explored via catalyzed ethylene hydrogenation on supported platinum nanoclusters. *Nat. Commun.* **7**, 10389 (2016).
21. Liu, J.-C. et al. Heterogeneous Fe3 single-cluster catalyst for ammonia synthesis via an associative mechanism. *Nat. Commun.* **9** (2018). https://doi.org/10.1038/s41467-018-03795-8
22. Tian, S. et al. Dual-atom Pt heterogeneous catalyst with excellent catalytic performances for the selective hydrogenation and epoxidation. *Nat. Commun.* **12**, 3181 (2021).
23. Lei, Y. et al. Increased Silver Activity for Direct Propylene Epoxidation via Subnanometer Size Effects. *Science* **328**, 224–228 (2010).

24. Mistry, H., Varela, A. S., Kühl, S., Strasser, P. & Cuenya, B. R. Nanostructured electrocatalysts with tunable activity and selectivity. *Nat. Rev. Mater.* **1** (2016). https://doi.org/10.1038/natrevmats.2016.9
25. Liu, L. C. et al. Evolution and stabilization of subnanometric metal species in confined space by in situ TEM. *Nat. Commun.* **9**, 574 (2018).
26. Yao, C. et al. Atomically precise dopant-controlled single cluster catalysis for electrochemical nitrogen reduction. *Nat. Commun.* **11** (2020). https://doi.org/10.1038/s41467-020-18080-w
27. Zhang, Z. S., Zandkarimi, B. & Alexandrova, A. N. Ensembles of metastable states govern heterogeneous catalysis on dynamic interfaces. *Acc. Chem. Res.* **53**, 447–458 (2020).
28. Kaden, W. E., Wu, T., Kunkel, W. A. & Anderson, S. L. Electronic structure controls reactivity of size-selected Pd clusters adsorbed on TiO2 surfaces. *Science* **326**, 826–829 (2009).
29. Liao, V., Cohen, M., Wang, Y. & Vlachos, D. G. Deducing sub-nanometer cluster size and shape distributions of heterogeneous supported catalysts. *Nat. Commun.* **14**, 1965 (2023).
30. Moliner, M. et al. Reversible transformation of pt nanoparticles into single atoms inside high-silica chabazite zeolite. *J. Am. Chem. Soc.* **138**, 15743–15750 (2016).
31. Kumari, S., Alexandrova, A. N. & Sautet, P. Nature of zirconia on a copper inverse catalyst under CO2 hydrogenation conditions. *J. Am. Chem. Soc.* **145**, 26350–26362 (2023).
32. Yan, G. et al. Reaction product-driven restructuring and assisted stabilization of a highly dispersed Rh-on-ceria catalyst. *Nat. Catal.* **5**, 119–127 (2022).
33. Wang, Y. G., Mei, D., Glezakou, V. A., Li, J. & Rousseau, R. Dynamic formation of single-atom catalytic active sites on ceria-supported gold nanoparticles. *Nat. Commun.* **6**, 6511 (2015).
34. Mitchell, S. & Pérez-Ramírez, J. Atomically precise control in the design of low-nuclearity supported metal catalysts. *Nat. Rev. Mater.* **6**, 969–985 (2021).
35. Wang, Y., Kalscheur, J., Su, Y.-Q., Hensen, E. J. M. & Vlachos, D. G. Real-time dynamics and structures of supported subnanometer catalysts via multiscale simulations. *Nat. Commun.* **12** (2021). https://doi.org/10.1038/s41467-021-25752-8
36. Shi, X. et al. Dynamics of heterogeneous catalytic processes at operando conditions. *JACS Au* **1**, 2100–2120 (2021).
37. Poths, P., Vargas, S., Sautet, P. & Alexandrova, A. N. Thermodynamic equilibrium versus kinetic trapping: thermalization of cluster catalyst ensembles can extend beyond reaction time scales. *ACS Catal.* **14**, 5403–5415 (2024).
38. Zhang, Z., Masubuchi, T., Sautet, P., Anderson, S. L. & Alexandrova, A. N. Hydrogen evolution on electrode-supported Ptn clusters: Ensemble of hydride states governs the size dependent reactivity. *Angew. Chem. Int. Ed.* **62** (2023). https://doi.org/10.1002/anie.202218210
39. Munarriz, J., Zhang, Z., Sautet, P. & Alexandrova, A. N. Graphite-supported Ptn cluster electrocatalysts: Major change of active sites as a function of the applied potential. *ACS Catal.* **12**, 14517–14526 (2022).
40. Poths, P. & Alexandrova, A. N. Theoretical perspective on operando spectroscopy of fluxional nanocatalysts. *J. Phys. Chem. Lett.* **13**, 4321–4334 (2022).
41. Konsolakis, M. The role of Copper–Ceria interactions in catalysis science: Recent theoretical and experimental advances. *Appl. Catal., B* **198**, 49–66 (2016).
42. Wang, W. W. et al. Crystal plane effect of ceria on supported copper oxide cluster catalyst for CO oxidation: Importance of metal-support interaction. *ACS Catal.* **7**, 1313–1329 (2017).
43. Ouyang, R., Curtarolo, S., Ahmetcik, E., Scheffler, M. & Ghiringhelli, L. M. SISSO: A compressed-sensing method for identifying the best low-dimensional descriptor in an immensity of offered candidates. *Phys. Rev. Mater.* **2**, 083802 (2018).
44. Davo-Quinonero, A. et al. Insights into the oxygen vacancy filling mechanism in CuO/CeO2 catalysts: A key step toward high selectivity in preferential CO oxidation. *ACS Catal.* **10**, 6532–6545 (2020).
45. Mishra, A. K., Roldan, A. & de Leeuw, N. H. CuO surfaces and CO2 activation: A dispersion-corrected DFT plus U study. *J. Phys. Chem. C.* **120**, 2198–2214 (2016).
46. Mishra, A. K., Roldan, A. & de Leeuw, N. H. A density functional theory study of the adsorption behavior of CO2 on Cu2O surfaces. *J. Chem. Phys.* **145** (2016). https://doi.org/10.1063/1.4958804
47. Dong, F., Meng, Y., Han, W., Zhao, H. & Tang, Z. Morphology effects on surface chemical properties and lattice defects of Cu/CeO2 catalysts applied for low-temperature CO oxidation. *Sci. Rep.* **9** (2019). https://doi.org/10.1038/s41598-019-48606-2
48. Wang, F. et al. In situ EPR study of the redox properties of CuO–CeO2 catalysts for preferential CO oxidation (PROX). *ACS Catal.* **6**, 3520–3530 (2016).
49. Su, Y. et al. Fabrication of Cu-doped CeO2 catalysts with different dimension pore structures for CO catalytic oxidation. *Catal. Surv. Asia* **20**, 231–240 (2016).
50. Zhou, Z., Zhang, J. & Liu, Y. Promoted low-temperature CO oxidation activity of CeO2 by Cu doping: The important role of oxygen vacancies. *Fuel* **359**, 130434 (2024).
51. Xia, Y. et al. Role of two-electron defects on the CeO2 surface in CO preferential oxidation over CuO/CeO2 catalysts. *ACS Sustain. Chem. Eng.* **7**, 18421–18433 (2019).
52. Lykaki, M. et al. Ceria nanoparticles shape effects on the structural defects and surface chemistry: Implications in CO oxidation by Cu/CeO2 catalysts. *Appl Catal. B-Environ.* **230**, 18–28 (2018).
53. Jia, A.-P., Jiang, S.-Y., Lu, J.-Q. & Luo, M.-F. Study of catalytic activity at the CuO–CeO2 interface for CO oxidation. *J. Phys. Chem. C.* **114**, 21605–21610 (2010).
54. Liu, B. L. et al. Optimum balance of Cu+ and oxygen vacancies of CuOx-CeO2 composites for CO oxidation based on thermal treatment. *Eur. J. Inorg. Chem.*, 1714-1723 (2019).
55. Xie, Y. et al. Structural origin of high catalytic activity for preferential CO oxidation over CuO/CeO2 nanocatalysts with different shapes. *Appl Catal. B-Environ.* **239**, 665–676 (2018).
56. Ding, J. et al. Engineering CeO2 configurations to regulate the CuO dispersion and switch pathways of preferential CO oxidation. *Appl. Catal., B* **331** (2023). https://doi.org/10.1016/j.apcatb.2023.122686
57. Adak, S. et al. In situ experimental and computational approach to investigate the nature of active site in low-temperature CO-PROX over CuOx-CeO2 catalyst. *Appl. Catal., A* **624** (2021). https://doi.org/10.1016/j.apcata.2021.118305
58. Hafner, J. Ab initio simulations of materials using VASP: Density-functional theory and beyond. *J. Comput. Chem.* **29**, 2044–2078 (2008).
59. Blochl, P. E. Projector augmented-wave method. *Phys. Rev. B* **50**, 17953–17979 (1994).
60. Perdew, J. P., Burke, K. & Ernzerhof, M. Generalized gradient approximation made simple. *Phys. Rev. Lett.* **77**, 3865–3868 (1996).
61. Pack, J. D. & Monkhorst, H. J. Special points for brillouin-zone integrations. *Phys. Rev. B* **16**, 1746–1747 (1977).
62. Loschen, C. et al. U study of cerium oxides: Dependence on the effective U parameter. *Phys. Rev. B* **75**, 035115 (2007).
63. Wu, D. X., Zhang, Q. M. & Tao, M. LSDA+U study of cupric oxide: Electronic structure and native point defects. *Phys. Rev. B* **73**, 235206 (2006).
64. Kolsbjerg, E. L., Groves, M. N. & Hammer, B. An automated nudged elastic band method. *J. Chem. Phys.* **145**, 094107 (2016).
65. Lindgren, P., Kastlunger, G. & Peterson, A. A. Scaled and dynamic optimizations of nudged elastic bands. *J. Chem. Theory Comput.* **15**, 5787–5793 (2019).

66. Smidstrup, S., Pedersen, A., Stokbro, K. & Jonsson, H. Improved initial guess for minimum energy path calculations. *J. Chem. Phys.* **140**, 214106 (2014).
67. Henkelman, G., Uberuaga, B. P. & Jonsson, H. A climbing image nudged elastic band method for finding saddle points and minimum energy paths. *J. Chem. Phys.* **113**, 9901–9904 (2000).
68. Heyden, A., Bell, A. T. & Keil, F. J. Efficient methods for finding transition states in chemical reactions: Comparison of improved dimer method and partitioned rational function optimization method. *J. Chem. Phys.* **123**, 224101 (2005).
69. Henkelman, G. & Jonsson, H. A dimer method for finding saddle points on high dimensional potential surfaces using only first derivatives. *J. Chem. Phys.* **111**, 7010–7022 (1999).
70. Sun, K. J., Zhao, Y. H., Su, H. Y. & Li, W. X. Force reversed method for locating transition states. *Theor. Chem. Acc.* **131**, 1118 (2012).
71. Evans, D. J. & Holian, B. L. The nose–hoover thermostat. *J. Chem. Phys.* **83**, 4069–4074 (1985).
72. Tang, W., Sanville, E. & Henkelman, G. A grid-based Bader analysis algorithm without lattice bias. *J. Phys. Condens. Matter* **21** (2009). https://doi.org/10.1088/0953-8984/21/8/084204
73. Dronskowski, R. & Blochl, P. E. Crystal orbital hamilton populations (Cohp) - energy-resolved visualization of chemical bonding in solids based on density-functional calculations. *J. Phys. Chem.* **97**, 8617–8624 (1993).
74. Deringer, V. L., Tchougreeff, A. L. & Dronskowski, R. Crystal orbital hamilton population (COHP) analysis as projected from plane-wave basis sets. *J. Phys. Chem. A* **115**, 5461–5466 (2011).
75. Zhang, Y. L., Hu, C. & Jiang, B. Embedded atom neural network potentials: Efficient and accurate machine learning with a physically inspired representation. *J. Phys. Chem. Lett.* **10**, 4962–4967 (2019).
76. Chen, J.-L., Liu, J.-X. & Li, W.-X. Collectivity effect in cluster catalysis under operational conditions. https://zenodo.org/records/16963396 (2025).

Acknowledgements

This work was supported by the Key Technologies R&D Program of China (2021YFA1502804), the Strategic Priority Research Program of the Chinese Academy of Science (XDB0450102), the National Natural Science Foundation of China (22172150, 22222306, 22221003, and 22432004), the National Natural Science Foundation of Anhui Province (2108085QB62), the USTC Research Funds of the Double First-Class Initiative (YD2060002012), the Innovation Program for Quantum Science and Technology (2021ZD0303302), the Fundamental Research Funds for the Central Universities (20720220009), the AI-driven experiments, simulations and model training were performed on the robotic AI-Scientist platform of the Chinese Academy of Science and high-performance computational resources provided by the University of Science and Technology of China and Hefei Advanced Computing Center. We thank Doc. Yaolong Zhang and Prof. Bin Jiang for support of the EANN package. We thank Michele Parrinello at the Italian Institute of Technology for reading the paper.

Author contributions

W.-X.L. and J.-X.L. led the conceptualization and design of the DFT calculations. J.-L.C. contributed to the DFT calculations and data analysis. X.-C.J., L.F., J.Z., J.-W.Z. contributed analysis of data and discussion. All the authors participated in writing the manuscript and in the overall scientific interpretation.

Competing interests

The authors declare no competing interests.

Additional information

Supplementary information The online version contains supplementary material available at https://doi.org/10.1038/s41467-025-64187-3.

Correspondence and requests for materials should be addressed to Jin-Xun Liu or Wei-Xue Li.

Peer review information *Nature Communications* thanks the anonymous reviewers for their contribution to the peer review of this work. A peer review file is available.